

# Quantum Simulation of Antiferromagnetic Spin Chains in an Optical Lattice

Jonathan Simon, Waseem S. Bakr, Ruichao Ma, M. Eric Tai, Philipp M. Preiss, and Markus Greiner\*

*Department of Physics, Harvard University, Cambridge, Massachusetts, 02138, USA*

(Dated: January 14, 2013)

Understanding exotic forms of magnetism in quantum mechanical systems is a central goal of modern condensed matter physics, with implications from high temperature superconductors to spintronic devices. Simulating magnetic materials in the vicinity of a quantum phase transition is computationally intractable on classical computers due to the extreme complexity arising from quantum entanglement between the constituent magnetic spins. Here we employ a degenerate Bose gas confined in an optical lattice to simulate a chain of interacting *quantum* Ising spins as they undergo a phase transition. Strong spin interactions are achieved through a site-occupation to pseudo-spin mapping. As we vary an applied field, quantum fluctuations drive a phase transition from a paramagnetic phase into an antiferromagnetic phase. In the paramagnetic phase the interaction between the spins is overwhelmed by the applied field which aligns the spins. In the antiferromagnetic phase the interaction dominates and produces staggered magnetic ordering. Magnetic domain formation is observed through both in-situ site-resolved imaging and noise correlation measurements. By demonstrating a route to quantum magnetism in an optical lattice, this work should facilitate further investigations of magnetic models using ultracold atoms, improving our understanding of real magnetic materials.

Ensembles of quantum spins arranged on a lattice and coupled to one another through magnetic interactions constitute a paradigmatic model-system in condensed matter physics. Such systems produce a rich array of magnetically-ordered ground states such as paramagnets, ferromagnets and antiferromagnets. Certain geometries and interactions induce competition between these orderings in the form of frustration, resulting in spin liquids[1] and spin glasses[2], as well as phases with topological order[3]. Varying system parameters can induce quantum phase transitions between the various phases[4]. A deeper understanding of the competition and resulting transitions between magnetic phases would provide valuable insights into the properties of complex materials such as high-temperature superconductors[5], and more generally into the intricate behaviours that can emerge when many simple quantum mechanical objects interact with one another.

Studying quantum phase transitions of magnetic condensed matter systems is hindered by the complex structure and interactions present in such systems, as well as the difficulty of controllably varying system parameters. With a few notable exceptions[6, 7], these issues make it difficult to capture the physics of such systems with simple models. Accordingly, there is a growing effort underway to realize condensed matter simulators using cold atom systems[8, 9] which are understood from first principles. The exquisite control afforded by cold atom experiments permits adiabatic tuning of such systems through quantum phase transitions[9, 10], enabling investigations of criticality[11, 12] and scaling[13]. Time-resolved local readout[14–16] and manipulation[17] provide direct access to local dynamics and correlations. With this powerful toolbox in hand, considerable attention has turned to understanding magnetic phase transitions using cold atom quantum simulations.

Initial experimental efforts to observe quantum magnetism have focused on bulk itinerant systems of ultracold fermions[18] and small, highly connected spin-networks simulated with ion chains[19]. Polar molecules[20] and Rydberg atoms[21] have been the subject of preliminary investigations both experimentally and theoretically[22–24] as alternatives to ground-state atoms with stronger, longer-range interactions. There has also been initial success in detecting ordered states which are artificially prepared through patterned loading[18, 25–27] and double-well[28] experiments.

In this work, we simulate a 1D chain of interacting Ising spins by mapping doublon-hole excitations of a Mott insulator[10, 29, 30] of spinless bosons in a tilted 1D optical lattice[31] onto a pseudo-spin degree of freedom. This is in contrast to the commonly considered approach in which the magnetic spins are represented by two internal states of the atoms, and nearest-neighbor spin-spin interactions result from super-exchange couplings[32]. Super-exchange interactions in cold atoms are quite weak, though they have been successfully observed in double well systems[33]. The approach presented here has the benefit of a dynamical timescale set by the tunneling rate  $t$ , rather than the super-exchange interaction  $t^2/U$ , where  $U$  is the onsite interaction energy. Combining the faster dynamics with the high spatial resolution afforded by a quantum gas microscope[14], we are able to directly observe transitions between paramagnetic and antiferromagnetic phases as spin-spin interactions compete with applied fields.

One of the primary concerns in studying transitions to magnetic states in cold atomic gases is the apparent difficulty of reaching the requisite temperatures[34]. These spin temperatures are at the edge of experimental reach[35, 36], and further cooling of lattice-spins remains an active field of research[37]. However, ultracold gases

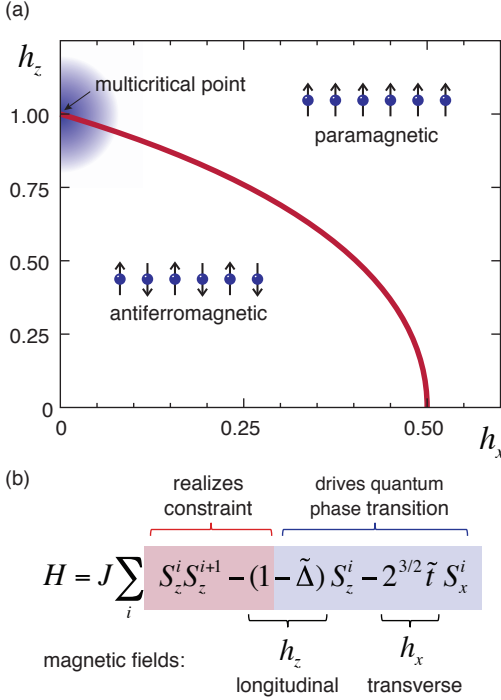


FIG. 1. **Spin model and its phase diagram.** **a.** An antiferromagnetic 1D Ising chain in longitudinal ( $h_z$ ) and transverse ( $h_x$ ) magnetic fields exhibits two phases at zero temperature[39, 40]. For weak applied fields the interactions between the spins drive the system to form an antiferromagnet. For strong applied fields the spins align to the field and produce a paramagnet. These two phases are separated by a second order phase transition (red line), except at the multicritical point  $(h_z, h_x) = (1, 0)$ , where the lack of a transverse field makes the transition classical and first order. The region that can be accessed in our experiment, in the vicinity of  $(h_z, h_x) = (1, 0)$ , is highlighted in blue. **b.** In this neighborhood the Hamiltonian may be decomposed into a constraint term that prevents adjacent spin-flips (red highlight), and fields that drive the phase transition (blue highlight).

in optical lattices are effectively isolated from their environment, and as such it is entropy and not temperature which is constant as system parameters are tuned. Spin-polarized Mott insulators have been demonstrated with defect densities approaching the percent level[15, 16], corresponding to configurational entropy far below the spin entropy required for magnetic ordering (see SI). This allows us to use such a Mott insulator to initialize a magnetic system with low spin entropy. We engineer a magnetic Hamiltonian whose paramagnetic ground state possesses good overlap with the initial Mott state, and subsequently tune it through a quantum phase transition[38] to produce an antiferromagnetic state. The difficulty of cooling lattice spins is thus replaced with the necessity of performing sufficiently slow adiabatic ramps to minimize diabatic crossings of manybody energy gaps.

## Ising Interactions in a Tilted Optical Lattice

The quantum Ising model is a paradigmatic model of magnetism, and an Ising chain is one of the simplest many-body systems to exhibit a quantum phase transition. The Hamiltonian describing a 1D antiferromagnetic Ising chain in the presence of an applied magnetic field is given by:

$$H = J \sum_i (S_z^i S_z^{i+1} - h_z S_z^i - h_x S_x^i)$$

Here  $S_z^i$  ( $S_x^i$ ) is the  $z$  ( $x$ ) spin-projection operator at site  $i$ , and  $h_z$  ( $h_x$ ) is the  $z$  ( $x$ )-component of the magnetic field applied to site  $i$ . The zero temperature phase diagram of the model[39, 40] is shown in Fig. 1a, for a homogeneous applied field  $(h_z, h_x)$ . For small applied fields, the magnetic interactions induce staggered ordering of the spins, producing an antiferromagnet (AF). For large applied fields, the field overwhelms the interactions, and all spins align to the field, producing a paramagnet (PM).

Our approach to constructing a magnetic Hamiltonian was proposed by Sachdev *et al.*[31], in the context of experiments by Greiner *et al.*[10], where a gradient was applied to measure the insulating properties of the Mott state. Sachdev *et al.* showed that under the influence of such field gradients, the dynamics of a 1D Mott insulator map onto the aforementioned Ising model (see Methods) in the neighborhood of  $(h_z, h_x) = (1, 0)$  (Fig. 1b).

In the Mott insulator regime ( $U \gg t$ ) it is energetically forbidden for the atoms to tunnel as long as the tilt per lattice site,  $E$ , differs from the onsite atom-atom interaction  $U$ . Hence, the system remains in a state with one atom per lattice site for  $E < U$  (Fig. 2a). As the tilt approaches the interaction strength ( $E = U$ ), each atom is free to tunnel onto its neighbor, so long as its neighbor has not itself tunneled (Fig. 2b). This nearest-neighbor constraint is the source of the effective spin-spin interaction. If the tilt  $E$  is increased sufficiently slowly through the transition so as to keep the system near the many-body ground state, density wave ordering results (Fig. 2c).

The mapping onto a spin-1/2 model arises as each atom has only two possible positions: an atom that has not tunneled corresponds to an “up” spin, and an atom that has tunneled corresponds to a “down” spin. Fig. 2d shows the spin configurations that correspond to various atom distributions in the optical lattice. The transition from a uniform phase at small tilt to a density wave phase at large tilt then corresponds to a transition from a paramagnetic phase to an antiferromagnetic phase in the spin model. The longitudinal field  $h_z$  thus arises from the lattice tilt, and the transverse field  $h_x$  from tunneling. As derived in the Methods, the mapping between Bose-Hubbard and spin models is given by

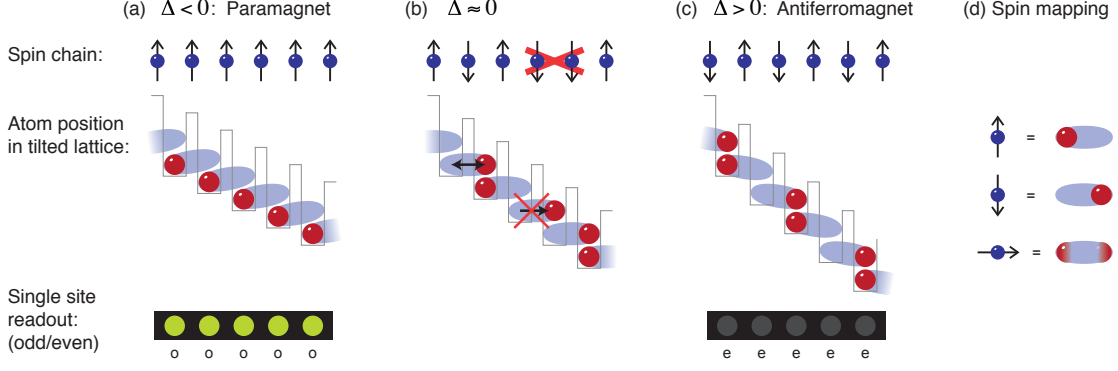


FIG. 2. **Tilted Hubbard model and mapping to spin model.** **a.** Middle row: When a Mott insulator is placed in a tilted lattice, it remains in a state with one atom per lattice site until the tilt per site  $E$  reaches the onsite interaction energy  $U$ . **b.** At this point the energy cost  $\Delta = E - U$  to move to the neighboring site vanishes, and the atoms begin to tunnel resonantly to reduce their energy. An atom, however, can only tunnel to a neighboring site if the atom on that site has not itself tunneled away. If no atom is present on the neighboring site, the tunneling process is suppressed by the energy gap  $U$ . This creates a strong constraint and leads to the formation of entangled states. **c.** As the tilt is increased further, the system transitions into a doubly degenerate staggered phase. **d.** This system may be mapped onto a model of interacting spin-1/2 particles, where the two spin states correspond to the two possible positions of each atom. In the spin model, the aforementioned constraint forbids adjacent down spins, realizing a spin-spin interaction. The initial Mott insulator now corresponds to a paramagnetic phase with all spins aligned upwards to a large magnetic field (see top row), the state at resonant tilt corresponds to a non-trivial (critical) spin configuration, and staggered ordering at even larger tilt corresponds to an anti-ferromagnetic phase. Bottom row: The phases can be detected by single lattice site imaging. Because the imaging system is sensitive only to the parity of the atom number, paramagnetic domains appear bright **a.**, and anti-ferromagnetic domains appear dark **c.**

$(h_z, h_x) = (1 - \tilde{\Delta}, 2^{3/2}\tilde{t})$ ,  $\tilde{t} = t/J$ ,  $\tilde{\Delta} = \Delta/J = (E - U)/J$ , with  $t$  the single-particle tunneling rate, and  $J \sim U$  the constraint term.

Spatially varying tilts in the optical lattice can give rise to site-to-site variation of  $h_z$ . Such inhomogeneity would impact the critical behaviour by breaking the translational symmetry, inducing different sites to transition at different applied tilts. Accordingly, the resulting many-body energy gaps, dynamical timescales[41, 42], and entropy of entanglement[43] would differ from the homogeneous case. Controlling such inhomogeneities is thus crucial for studies of magnetism.

The mapping of the Hubbard model onto the spin-model breaks down away from  $(h_z, h_x) \sim (1, 0)$ . This is because states with three atoms on a lattice site are not within the Hilbert space that maps to the spin model. As such we can study ground state dynamics and low-energy excitations of the equivalent Ising model, but not high-energy excitations associated with adjacent flipped spins. These constraints admit investigation of the Ising physics only in the neighborhood of the multi-critical point  $(h_z, h_x) \sim (1, 0)$ . This regime is of particular theoretical interest as the model is here not exactly solvable[39]. It is nonetheless in the Ising universality class[31], and so a study of its critical physics would provide insight into the behaviours of the more commonly considered transverse ( $h_z = 0$ ) Ising model.

### Extracting Spin Observables

We locally detect magnetic ordering by utilizing our quantum gas microscope, capable of resolving individual lattice sites. The microscope is sensitive only to the parity of the site occupation number[14], and so PM domains (with one atom per lattice site) should appear as entirely bright regions, and AF domains (with alternating 0-2-0-2 occupation) as entirely dark regions. In the spin language, the detection parity operator  $P^i$  measures the spin-spin correlation between adjacent spins:

$$P^i = 4S_z^{i-1}S_z^i$$

Throughout this article we will characterize our spin-ordering primarily via the probability that site  $i$  has odd occupation  $p_{\text{odd}}^i = \frac{1}{2}(1 + \langle P^i \rangle)$ . Taking the spin constraint into account, the chain average of  $p_{\text{odd}}^i$  is equivalent to a chain-averaged measurement of  $\langle S_z^i \rangle$ , the mean  $z$ -projection of the spin:  $\langle S_z^i \rangle = \frac{1}{2}p_{\text{odd}}^i$ . Here angle brackets denote realization-averages and bars denote chain-averages.

This parity measurement allows us to locally identify magnetic domains and estimate their size. This, however, is not a direct measurement of the AF order parameter described in Ref. [31], and does not reflect the broken symmetry in the AF phase (see Methods). Accordingly, we also study the AF order parameter more directly through 1D quantum noise interferometry[44].

## Observing the Phase Transition

Our experiments begin with a Mott insulator of  $^{87}\text{Rb}$  atoms in a two dimensional optical lattice with spacing  $a = 680\text{ nm}$  and a depth of  $35E_r$ , in the focal plane of a high resolution imaging system which allows detection of single atoms on individual lattice sites as described in previous work[14, 15]. The lattice recoil energy is given by  $E_r = \hbar^2/8ma^2$ , where  $\hbar$  is Planck's constant and  $m$  the mass of  $^{87}\text{Rb}$ . We generate our effective  $h_z$  by tilting the lattice potential by  $E$  per lattice-site, which is achieved via a magnetic field gradient along the  $x$ -direction (defined in Fig. 3a). This gradient is applied in two steps: first a fast ramp (in 8 ms) to just below the transition point[31, 39] at  $E = U + 1.85t$  ( $h_z = 1 - 0.66h_x$ ), followed by a slow linear ramp (in 250 ms) across the transition. Before starting the slow gradient ramp, the lattice depth along the  $y$ -direction is increased (in 2 ms) typically to  $45(7)E_r$ , while the depth along the  $x$ -direction is reduced to  $14(1)E_r$ . This decouples the system into 1D chains with significant tunneling only along their lengths. Simultaneously, we compensate the tilt inhomogeneity arising from harmonic confinement, leaving only residual inhomogeneity arising from our lattice projection method[14]. We then probe the system by stopping the ramp at various points and observing spin ordering, first of the entire cloud, and then specializing to the transitions of individual lattice sites in a particular chain.

We initiate the gradient ramp on the paramagnetic side of the phase transition (typically at  $E/U = 0.7$ ), as the initial Mott state has good overlap with the paramagnetic ground state (Fig. 3ai). At the end of the ramp ( $E/U = 1.2$ ), we observe an even occupation with probability  $0.90(2)$  (Fig. 3aii), as expected for an AF phase in the magnetic model where the spin-spin interaction overwhelms the effective field  $h_z$ . In between, density-wave (AF) ordered regions begin to form, as shown in Fig. 3aiii. Fig. 3c shows  $p_{\text{odd}}$  at various times during this ramp. A crucial characteristic of an adiabatic transition is that it is *reversible*. Fig. 3b shows  $p_{\text{odd}}$  during a ramp from a PM to an AF and back. The recovery of the singly occupied sites is evidence of the reversibility of the process, and hence that the state at the end of the forward ramp is in fact an antiferromagnet.

We directly verify the existence of staggered ordering in the AF phase via a 1D quantum noise correlation measurement[44]. We perform this measurement by increasing the lattice depth along the chains to  $35E_r$  within 5 ms and then rapidly switching off that lattice to realize a 1D expansion. The resulting spatial autocorrelation is plotted in Fig. 3d at both the beginning (i) and end (ii) of the ramp from the PM phase to the AF phase. In the PM phase the spectrum exhibits peaks at momentum difference  $p = \hbar/a$ , characteristic of a Mott insulator[45]. In the AF phase peaks at  $p = \hbar/2a$  appear, indicative

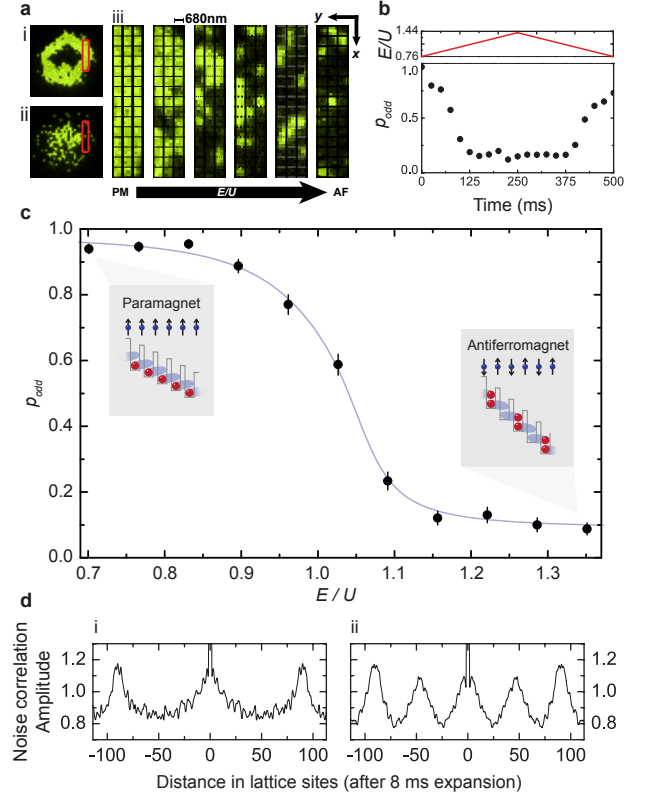


**FIG. 3. Probing the paramagnet to antiferromagnet phase transition.** **a.** Representative single-shot images as the tilt is swept adiabatically through the phase transition in 250 ms. The upper image (i) is near-perfect  $n = 1$  (bright) and  $n = 2$  (center dark) Mott insulator shells in PM phase. The lower image (ii) is the “inverted” shell structure characteristic of the staggered ordering of the AF phase after a tilt along the  $x$ -direction. The inversion occurs because chains of sites in a shell with  $N$  atoms per site are converted into a staggered phase wherein sites alternate between  $N - 1$  and  $N + 1$  atoms, and so a shell with even occupation becomes a region of odd occupation, and vice-versa. The remaining pictures (iii) are several chains (within the red rectangles in i and ii) of the  $N = 1$  shell at various points during the sweep,  $t = 0, 50, 100, 150, 175$  and  $250$  ms, showing AF domain formation. **b.** To demonstrate the reversibility of the transition, we adiabatically ramp from the PM phase into the AF phase and back in 500 ms. The probability that a site in the  $N = 1$  shell has odd occupation at various points during the ramp is observed to drop, and subsequently revive, as expected when the system leaves and then returns to the PM phase. **c.** A closer look at the PM to AF quantum phase transition within an  $N = 1$  shell, showing  $p_{\text{odd}}$  vs. tilt. Errorbars reflect  $1\sigma$  statistical errors in the region-averaged mean  $p_{\text{odd}}$ . The blue curve is a guide for the eye. **d.** Noise correlation measurement after 8 ms time of flight expansion along the chains. (i) In the PM phase, peaks at momentum  $\hbar/a$  correspond to a periodicity of one lattice site before expansion, characteristic of a Mott insulator[45]. (ii) In the AF phase, additional peaks at momentum  $\hbar/2a$  indicate the existence of staggered ordering, with a periodicity of two lattice sites.

of the emergence of a spatial ordering with twice the wavelength. In principle the mean domain size can be extracted from the  $p = h/2a$  peak width, however our measurement is broadened by both finite expansion time and aberration arising from the fact that the 1D expansion is performed not in free space but in slightly corrugated confining tubes.

### Single-Site Study of the Transition

A high resolution study reveals that in the presence of harmonic confinement the spins undergo the transition sequentially due to the resulting spatial variation of the effective longitudinal field. Fig. 4a shows  $p_{\text{odd}}$  vs. tilt for two different rows of a harmonically confined Mott insulator, separated by seven lattice sites. These two rows tune through resonance at different tilts, as can be understood from the energy level diagram Fig. 4b. To realize a homogeneous field Ising model we eliminate the harmonic confinement (see Methods) immediately before the slow ramp into the AF phase. The homogeneity is now only limited by residual lattice beam disorder, and accordingly, Fig. 4c demonstrates that different rows transition almost simultaneously, as anticipated theoretically (Fig. 4d).

After compensating the harmonic confinement, we use high resolution imaging to study the transition on the single-site level. This allows us to focus on a single six-site chain with particularly low inhomogeneity, which we will study for the remainder of this article. We identify such a chain by imaging individual lattice sites as the system is tuned across the PM-AF transition. Fig. 5 shows the average occupation of each of the six adjacent sites (black curves), versus tilt, for a 250 ms ramp across the transition. The r.m.s. variation in the fitted centers is 6 Hz, significantly less than their mean 10%–90% width of 105(30) Hz, corresponding to the effective transverse field  $2^{3/2}t = 28$  Hz. By quickly jumping across the transition with tunneling inhibited, and then ramping slowly across the transition in reverse with tunneling allowed (red curves, taken under slightly different conditions), we are able to rule out large, localized potential steps that would otherwise prevent individual spins from flipping. The curves in Fig. 5 provide our best estimate of the inhomogeneity. However, exact determination of the site-to-site disorder using this technique is complicated by the many-body nature of the observed transition. New spectroscopic techniques such as single-site modulation spectroscopy would need to be developed to ensure that the inhomogeneities are small enough to study criticality in long, homogeneous Ising chains.

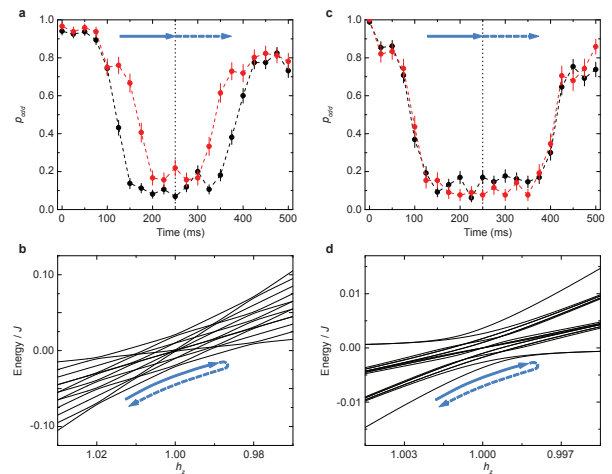


**FIG. 4. Impact of harmonic confinement.** For a ramp (see Fig. 3b) across the transition (in 250 ms) and back, **a.** harmonic confinement broadens the transition, inducing rows of the cloud seven lattice sites apart to undergo the transition at different applied tilts. **b.** Corresponding energy spectrum of a 1D Ising chain in a longitudinal field gradient of 0.01 per lattice site, reflecting seven spins and open boundary conditions. Each avoided crossing of the lowest energy state corresponds to a single spin-flip with energy gap  $h_x = 0.001$ . **c.** Once the confinement has been properly compensated, the average transition curves from the two rows overlap. Not apparent from these averaged curves is a small amount of residual tilt inhomogeneity. **d.** Energy spectrum for a homogeneous 1D Ising chain of six spins, with periodic boundary conditions. In contrast to **b.**, the single avoided crossing drives all spin-flips simultaneously, with a gap that decreases with increasing system size, as expected for the critical slowdown near a quantum phase transition. All errorbars are  $1\sigma$  statistical uncertainties derived from the mean of  $p_{\text{odd}}$  averaged over a region.

### Domain Formation in a 1D Ising Chain

Quantum fluctuations induce the formation of AF domains as the homogeneous chain is ramped through the transition. As discussed previously, these domains will appear as uninterrupted strings of dark lattice sites. Fig. 6a shows the observed mean length-weighted dark domain length extracted from 43 single-shot images per tilt, as the system is ramped from the PM phase into the AF phase. The dark domain length is here defined as the number of contiguous dark sites (see SI). On the AF side of the transition, the mean dark domain length grows to 4.9(2) sites, giving evidence that the average AF domain size approaches the system size.

We next investigate the impact of ramp rate on the transition from the PM phase into the AF phase in the homogeneous chain. The blue points in Fig. 6b show  $p_{\text{odd}}$  as a function of ramp speed across the transition, which may be understood qualitatively as the fraction of the system that has not transitioned into AF domains of



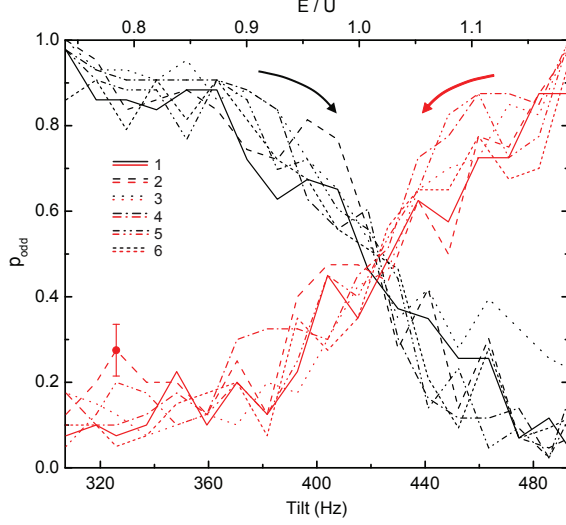


**FIG. 5. Site-resolved transition in near-homogeneous Ising model.** The probability of odd occupation of six individual lattice sites forming a contiguous 1D chain, versus the tilt, shown for both forward (black) and reverse (red) ramps. The spins transition at the same applied field to within the curve width, set by quantum fluctuations. A typical  $1\sigma$  statistical error bar is shown. The single-site widths are consistent with a longitudinal lattice depth of  $14(1)E_r$ , in agreement with a Kapitza-Dirac measurement of  $15(2)E_r$ . A large local potential step at a particular lattice would be reflected as a shift in either the forward or reverse  $p_{\text{odd}}$  curve at that site. The reverse curve demonstrates our ability to adiabatically prepare the highest energy state of the restricted spin Hamiltonian: the system exhibits PM ordering on the AF side of the transition, and AF ordering on the PM side of the transition.

any size. The time required to flip the spins is  $\sim 50$  ms, consistent with tunneling induced quantum fluctuations driving the transition. The black points in Fig. 6b are the mean length-weighted dark domain length as a function of ramp rate. As above, the mean dark domain length saturates at  $4.8(2)$ , near the system size of six sites. The remaining defects likely result from imperfect overlap of the initial MI with the PM state at finite  $\tilde{\Delta}$ , as well as defects of the initial MI and heating during the ramp.

While the antiferromagnetic domain formation discussed thus far occurs in spin-chains that remain in a quantum state near the many-body ground state, we can also produce antiferromagnetic domains that correspond to the highest energy state of the constrained Hilbert space. This is achieved by starting with the Mott insulator and rapidly ramping the field gradient through the transition point with tunneling inhibited, then adiabatically ramping back with tunneling permitted. This prepares a PM on the AF side of the transition, and adiabatically converts it into an AF on the PM side. The resulting data are shown in red, in Fig. 5 and Fig. 6a,

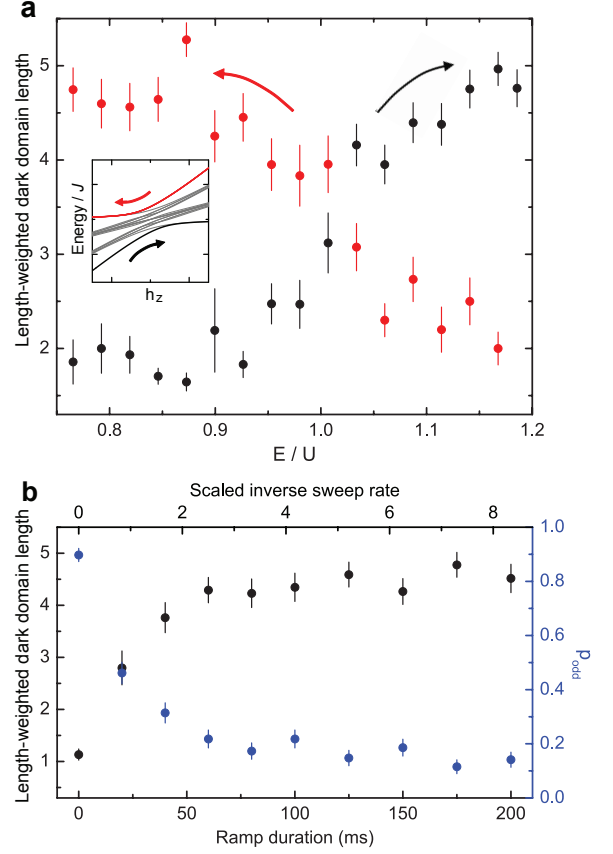


**FIG. 6. Dynamics of antiferromagnetic domain formation.** Within a single six-site chain with low disorder, **a.** shows the mean dark-domain length as a function of the tilt in units of  $U$ , for both forward (black) and reverse (red) ramps. As the system enters the AF phase the mean dark domain length grows until it approaches the chain length. Domain formation in the reverse ramp, beginning on the AF side of the transition, demonstrates the adiabatic generation of AF domains on the PM side of the transition, corresponding to the highest energy state of the spin Hamiltonian (inset). Within the same chain, **b.** shows  $p_{\text{odd}}$  (blue) and dark domain length (black) versus the duration  $T_{\text{ramp}}$  of the ramp from  $E/U = 0.7$  to  $E/U = 1.2$ . The top axis shows the scaled inverse sweep rate  $\alpha = 8\pi^2 t^2 / (\Delta E / T_{\text{ramp}})$ , where  $\Delta E$  is the sweep range in Hz, and  $t$  is the tunneling rate, in Hz, along the chain. The characteristic timescale for domain formation is  $\alpha \approx 2$ , or  $T_{\text{ramp}} \approx 50$  ms, indicating that tunneling along the chain is the source of the quantum fluctuations that drive domain formation. Errorbars for the dark chain lengths are  $1\sigma$  statistical uncertainties, arising from the number of detected domains of each length. Those for  $p_{\text{odd}}$  are the  $1\sigma$  statistical uncertainty in the mean of the six-site chain.

demonstrating that these high energy states are sufficiently long-lived to support domain formation. Similar ideas have been proposed for preparation of difficult-to-access many-body states using the highest energy states of Hamiltonians with easily prepared ground states[46].

## Conclusions and Outlook

We have experimentally realized a quantum simulation of an Ising chain in the presence of longitudinal and transverse fields. By varying the applied longitudinal field, we drive a transition between PM and AF phases, and verify the formation of spin domains via both direct *in situ* imaging, and noise-correlation in expansion. We study the adiabaticity requirements for transition dynamics, and observe a timescale consistent with tunneling-induced quantum fluctuations. By rapidly tuning through the transition and ramping back across it slowly, we prepare the highest energy state of a many-body spin Hamiltonian.

We introduce and implement a novel route to studying low entropy magnetism in optical lattices. Complexities associated with cooling of spin mixtures[35–37] are circumvented by employing a low entropy, gapped Mott insulator as an initially spin-polarized state, and then adiabatically opening a spin degree of freedom[38]. This recipe is directly applicable to more traditional approaches to quantum magnetism, including those employing super-exchange interactions[32].

The spin-mapping demonstrated here opens a new avenue for future work on quantum magnetism and control. Strong effective magnetic interactions make possible the creation of states with coherently generated long-range order. Combined with a lower-disorder lattice, in-depth studies of criticality become possible. Tilting by the band excitation energy will enable studies of the transverse Ising model[47]. It will be interesting to investigate the impact of various types of controlled disorder on criticality and transition dynamics, as well as the possible existence of non-thermalizing states[48]. A particularly intriguing direction is the extension of the tilted Mott insulator physics to higher dimensions. The simple square lattice geometry will provide access to phases with longitudinal density wave ordering and transverse superfluidity[31]. More sophisticated geometries will produce frustrated systems with novel quantum liquid and dimer covered ground states[49].

We would like to thank E. Demler, T. Kitagawa, M. D. Lukin, S. Pielawa, and S. Sachdev for stimulating discussions. This work was supported by grants from the Army Research Office with funding from the DARPA OLE program, an AFOSR MURI program, and by grants from the NSF.

---

\* greiner@physics.harvard.edu

- [1] L. Balents, *Nature* **464**, 199 (2010).
- [2] K. Binder and A. P. Young, *Rev. Mod. Phys.* **58**, 801 (1986).
- [3] A. Kitaev, *Annals of Physics* **321**, 2 (2006).
- [4] S. Sachdev, *Quantum Phase Transitions* (Cambridge University Press, 2000).
- [5] P. W. Anderson, *Science* **235**, 1196 (1987).
- [6] C. Rüegg, B. Normand, M. Matsumoto, A. Furrer, D. F. McMorrow, K. W. Krämer, H. U. Güdel, S. N. Gvasaliya, H. Mutka, and M. Boehm, *Phys. Rev. Lett.* **100**, 205701 (2008).
- [7] R. Coldea, D. A. Tennant, E. M. Wheeler, E. Wawrzynska, D. Prabhakaran, M. Telling, K. Habicht, P. Smeibidl, and K. Kiefer, *Science* **327**, 177 (2010).
- [8] M. Lewenstein, A. Sanpera, V. Ahufinger, B. Damski, A. Sen, and U. Sen, *Adv. Phys.* **56**, 243 (2007).
- [9] I. Bloch, J. Dalibard, and W. Zwerger, *Rev. Mod. Phys.* **80**, 885 (2008).
- [10] M. Greiner, O. Mandel, T. Esslinger, T. W. Hänsch, and I. Bloch, *Nature* **415**, 39 (2002).
- [11] S. Sachdev, *Nature Physics* **4**, 173 (2008).
- [12] X. Zhang, C. Hung, S. Tung, N. Gemelke, and C. Chin, (2010), arXiv:cond-mat/1101.0284.
- [13] C. Hung, X. Zhang, N. Gemelke, and C. Chin, (2010), arXiv:cond-mat/1009.0016.
- [14] W. S. Bakr, J. I. Gillen, A. Peng, S. Fölling, and M. Greiner, *Nature* **462**, 74 (2009).
- [15] W. S. Bakr, A. Peng, M. E. Tai, R. Ma, J. Simon, J. I. Gillen, S. Fölling, L. Pollet, and M. Greiner, *Science* **329**, 547 (2010).
- [16] J. F. Sherson, C. Weitenberg, M. Endres, M. Cheneau, I. Bloch, and S. Kuhr, *Nature* **467**, 68 (2010).
- [17] C. Weitenberg, M. Endres, J. F. Sherson, M. Cheneau, P. Schauß, T. Fukuhara, I. Bloch, and S. Kuhr, (2011), arXiv:cond-mat/1101.2076.
- [18] G. Jo, Y. Lee, J. Choi, C. A. Christensen, T. H. Kim, J. H. Thywissen, D. E. Pritchard, and W. Ketterle, *Science* **325**, 1521 (2009).
- [19] K. Kim, M. Chang, S. Korenblit, R. Islam, E. E. Edwards, J. K. Freericks, G. Lin, L. Duan, and C. Monroe, *Nature* **465**, 590 (2010).
- [20] K. Ni, S. Ospelkaus, M. H. G. de Miranda, A. Pe'er, B. Neyenhuis, J. J. Zirbel, S. Kotochigova, P. S. Julienne, D. S. Jin, and J. Ye, *Science* **322**, 231 (2008).
- [21] R. Heidemann, U. Raitzsch, V. Bendkowsky, B. Butscher, R. Löw, L. Santos, and T. Pfau, *Phys. Rev. Lett.* **99**, 163601 (2007).
- [22] M. D. Lukin, M. Fleischhauer, R. Cote, L. M. Duan, D. Jaksch, J. I. Cirac, and P. Zoller, *Phys. Rev. Lett.* **87**, 037901 (2001).
- [23] H. P. Büchler, E. Demler, M. Lukin, A. Micheli, N. Prokof'ev, G. Pupillo, and P. Zoller, *Phys. Rev. Lett.* **98**, 060404 (2007).
- [24] H. Weimer, M. Müller, I. Lesanovsky, P. Zoller, and H. P. Büchler, *Nature Physics* **6**, 382 (2010).
- [25] P. J. Lee, M. Anderlini, B. L. Brown, J. Sebby-Strabley, W. D. Phillips, and J. V. Porto, *Phys. Rev. Lett.* **99**, 020402 (2007).
- [26] S. Fölling, *Probing strongly correlated states of ultracold atoms in optical lattices*, Ph.D. thesis, Johannes-Gutenberg-Universität Mainz (2008).
- [27] P. Soltan-Panahi, J. Struck, P. Hauke, A. Bick, W. Plenkers, G. Meineke, C. Becker, P. Windpassinger, M. Lewenstein, and K. Sengstock, (2010), arXiv:cond-mat/1005.1276.
- [28] S. Fölling, S. Trotzky, P. Cheinet, M. Feld, R. Saers, A. Widera, T. Müller, and I. Bloch, *Nature* **448**, 1029 (2007).

- [29] M. P. A. Fisher, P. B. Weichman, G. Grinstein, and D. S. Fisher, Phys. Rev. B **40**, 546 (1989).
- [30] D. Jaksch, C. Bruder, J. I. Cirac, C. W. Gardiner, and P. Zoller, Phys. Rev. Lett. **81**, 3108 (1998).
- [31] S. Sachdev, K. Sengupta, and S. M. Girvin, Phys. Rev. B **66**, 075128 (2002).
- [32] L. Duan, E. Demler, and M. D. Lukin, Phys. Rev. Lett. **91**, 090402 (2003).
- [33] S. Trotzky, P. Cheinet, S. Fölling, M. Feld, U. Schnorrberger, A. M. Rey, A. Polkovnikov, E. A. Demler, M. D. Lukin, and I. Bloch, Science **319**, 295 (2008).
- [34] B. Capogrosso-Sansone, Ş. G. Söyler, N. V. Prokof'ev, and B. V. Svistunov, (2009), phys. Rev. A **81**, 053622 (2010), arXiv:cond-mat/0912.1865.
- [35] D. M. Weld, P. Medley, H. Miyake, D. Hucul, D. E. Pritchard, and W. Ketterle, Phys. Rev. Lett. **103**, 245301 (2009).
- [36] P. Medley, D. M. Weld, H. Miyake, D. E. Pritchard, and W. Ketterle, (2010), arXiv:cond-mat/1006.4674.
- [37] D. McKay and B. DeMarco, (2010), arXiv:cond-mat/1010.0198.
- [38] J. J. García-Ripoll, M. A. Martin-Delgado, and J. I. Cirac, Phys. Rev. Lett. **93**, 250405 (2004).
- [39] A. A. Ovchinnikov, D. V. Dmitriev, V. Y. Krivnov, and V. O. Cheranovskii, Phys. Rev. B **68**, 214406 (2003).
- [40] M. Novotny and D. Landau, Journal of Magnetism and Magnetic Materials **54-57**, 685 (1986).
- [41] Y. Imry and S. Ma, Phys. Rev. Lett. **35**, 1399 (1975).
- [42] J. Dziarmaga, Phys. Rev. B **74**, 064416 (2006).
- [43] G. Vidal, J. I. Latorre, E. Rico, and A. Kitaev, Phys. Rev. Lett. **90**, 227902 (2003).
- [44] E. Altman, E. Demler, and M. D. Lukin, Phys. Rev. A **70**, 013603 (2004).
- [45] S. Fölling, F. Gerbier, A. Widera, O. Mandel, T. Gericke, and I. Bloch, Nature **434**, 481 (2005).
- [46] A. S. Sørensen, E. Altman, M. Gullans, J. V. Porto, M. D. Lukin, and E. Demler, Phys. Rev. A **81**, 061603 (2010).
- [47] P. Plitz, P. Schlagheck, and S. Wimberger, Eur. Phys. J. D. , 1 (2010), 10.1140/epjd/e2010-10554-7.
- [48] M. C. Bañuls, J. I. Cirac, and M. B. Hastings, Phys. Rev. Lett. **106**, 050405 (2011).
- [49] S. Pielawa, T. Kitagawa, E. Berg, and S. Sachdev, (2011), arXiv:cond-mat/1101.2897.
- [50] D. Greif, L. Tarruell, T. Uehlinger, R. Jördens, and T. Esslinger, (2010), arXiv:cond-mat/1012.0845.
- [51] R. Jördens, N. Strohmaier, K. Gunter, H. Moritz, and T. Esslinger, Nature **455**, 204 (2008).
- [52] S. Will, T. Best, U. Schneider, L. Hackermüller, D. Luhmann, and I. Bloch, Nature **465**, 197 (2010).
- [53] P. R. Johnson, E. Tiesinga, J. V. Porto, and C. J. Williams, New Journal of Physics **11**, 093022 (2009).

## Methods

### Mapping onto the Spin Model

We follow Sachdev *et al.* in formally mapping a 1D Mott insulator of spinless bosons in a tilted lattice onto a chain of interacting dipoles (doublon-hole pairs, in a singly occupied Mott shell), and then onto a chain of spin-

1/2 particles with AF Ising interactions in longitudinal and transverse fields. In a homogeneously tilted lattice, the 1D Bose-Hubbard Hamiltonian reads:

$$H = -t \sum_j \left( a_j^\dagger a_{j+1} + a_j a_{j+1}^\dagger \right) + \frac{U}{2} \sum_j n_j (n_j - 1) - E \sum_j j \cdot n_j$$

Here  $t$  is the nearest-neighbor tunneling rate,  $U$  is the onsite interaction,  $E$  is the tilt per lattice site,  $a_j^\dagger$  ( $a_j$ ) is the creation (annihilation) operator for a particle on site  $j$ , and  $n_j = a_j^\dagger a_j$  is the occupation number operator on site  $j$ .

For a tilt near  $E = U$ , the onsite interaction energy cost for an atom to tunnel onto its neighbor is almost precisely cancelled by the tilt energy. If one starts in a Mott insulator with  $M$  atoms per site, an atom can then resonantly tunnel onto the neighboring site to produce a dipole excitation with a pair of sites with  $M + 1$  and  $M - 1$  atoms. The resonance condition is only met if adjacent sites contain equal numbers of atoms, so only one dipole can be created per link and neighboring links cannot both support dipoles. We define a (properly normalized) dipole creation operator  $d_j^\dagger = \frac{a_j a_{j+1}^\dagger}{\sqrt{M(M+1)}}$ .

The Bose-Hubbard Hamiltonian above can hence be mapped onto the dipole Hamiltonian:

$$H = -\sqrt{M(M+1)}t \sum_j \left( d_j^\dagger + d_j \right) + (U - E) \sum_j d_j^\dagger d_j$$

subject to the constraints  $d_j^\dagger d_j \leq 1$ ,  $d_{j+1}^\dagger d_{j+1} d_j^\dagger d_j = 0$ .

The factor of  $\sqrt{M(M+1)}$  arises due to bosonic enhancement.

To map from the dipole Hamiltonian to the spin-1/2 Hamiltonian, we define a link without (with) a dipole excitation to be an up (down) spin along  $\hat{z}$ . Then the creation/annihilation of dipoles are related to the flipping of spins, and we can write:

$$S_z^j = \frac{1}{2} - d_j^\dagger d_j, S_x^j = \frac{1}{2} \left( d_j^\dagger + d_j \right), \text{ and } S_y^j = \frac{i}{2} \left( d_j^\dagger - d_j \right)$$

The constraint forbidding adjacent dipoles can be implemented by introducing a positive energy term  $J d_{j+1}^\dagger d_{j+1} d_j^\dagger d_j$  to the Hamiltonian, where  $J$  is of order  $U$ . This term gives rise to nearest-neighbor interactions and an effective longitudinal field for the spins.

Defining  $\Delta = E - U$  the Hamiltonian for the spins now reads:

$$\begin{aligned} H &= J \sum_j S_z^j S_z^{j+1} - 2\sqrt{M(M+1)}t \sum_j S_x^j \\ &\quad - (J - \Delta) \sum_j S_z^j \\ &= J \sum_j \left( S_z^j S_z^{j+1} - h_x S_x^j - h_z S_z^j \right) \end{aligned}$$



The dimensionless fields are defined as  $h_x = 2^{3/2}t/J = 2^{3/2}\tilde{t}$ ,  $h_z = (1 - \frac{\Delta}{J}) = 1 - \tilde{\Delta}$ , with  $M$  set to one as in our experiment.

### Experimental Details

Our experiments start with a single layer 2D Mott insulator of  $^{87}\text{Rb}$  atoms in a  $35E_r$  lattice with 680 nm spacing as described in previous work. The atoms are in the  $|F = 1, m_f = -1\rangle$  state and the initial fidelity of the Mott insulator is 0.95(2), with local fidelities as high as 0.98. A magnetic field gradient along the  $x$ -direction is ramped up within 8 ms to tilt the lattice potential by  $0.7U$  per lattice site. At this point, the depth of the lattice along the chains is ramped down to  $14E_r$ , while the potential transverse to the chains is ramped up to  $45E_r$ , within 2 ms. At the same time, the optical potential providing harmonic confinement is ramped down. Tunneling between chains is negligible over the experimental timescale (see Supplementary notes for further discussion). The gradient is then ramped adiabatically through the transition point using a linear ramp that ends at a tilt of  $1.2U$  per lattice site, typically within 250 ms.

We can then perform either an *in situ* measurement or a 1D expansion of the chains to achieve noise correlation interferometry. In both cases, we use fluorescence imaging after pinning the atoms in a deep lattice to obtain the density distribution with single atom/single lattice-site resolution. Images far on the Mott side of the transition are used to select chains of atoms within the first shell of the insulator. The phase transition is then studied only within these chains, with quantitative curves employing data only from the single chain with lowest disorder.

For noise correlation measurements, the magnetic field gradient and the lattice along the chain are switched off, while the interchain lattice and the potential confining the atoms in the third direction remain on. After a 1D expansion for 8 ms, the atoms are pinned for imaging. To extract information about density wave ordering in the chains, several hundred images (250 for paramagnetic, 500 for antiferromagnetic phase) each containing 15 chains, are fitted to extract the atom positions, and then spatially autocorrelated and averaged as described in Ref. [26].

Lattice depths are calibrated to 15% using Kapitza-Dirac scattering, however the width of single-site transition regions was found to be a more sensitive probe of the longitudinal tunneling rate and hence the longitudinal lattice depth (see Supplementary Fig. S7), and accordingly was employed throughout this article.

The magnetic field gradient is calibrated using lattice modulation spectroscopy. In the presence of a potential gradient  $E$  per lattice site, modulation of the lattice depth along the chains causes resonant excitation at two

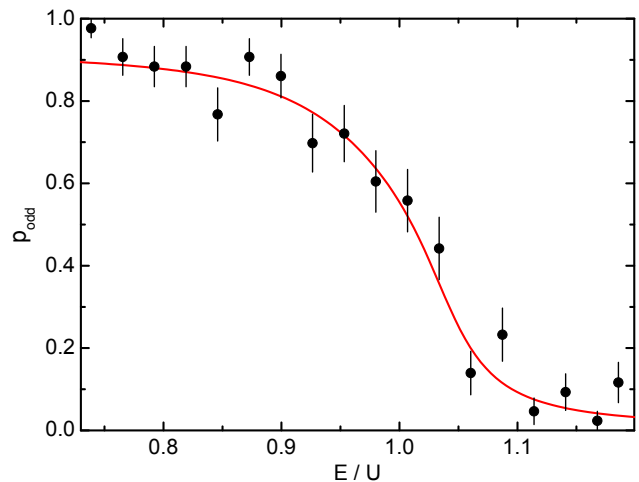


FIG. S7. **Single-site transition curve.** The occupation probability  $p_{\text{odd}}$  of a characteristic single site, plotted versus tilt as the system is ramped from the PM phase into the AF phase. The theory curve reflects a zero temperature exact diagonalization calculation of the ground state of a chain of six Ising spins (the shape of the  $p_{\text{odd}}$  curve is insensitive to chain length, see Supplementary Fig. S9), with periodic boundary conditions. The curve has been offset and rescaled vertically to account for defects arising from both the initial MI, and heating during the ramp. The theory allows us to extract a lattice depth of  $14(1)E_r$ . We attribute the residual fluctuations around the expected curve to residual oscillations reflecting non-adiabaticity arising from that fact that the ramp was initiated too close to the transition. The error bars are  $1\sigma$  statistical uncertainties.

frequencies,  $U + E$  and  $U - E$  corresponding to an atom in the Mott insulator moving up or down gradient. We detect these excitations as a reduction in the value of  $p_{\text{odd}}$  using in-situ imaging (see Supplementary Fig. S8). Using the mean of the two resonances, we obtain the interaction energy  $U = 430(20)$  Hz at  $16E_r$  longitudinal lattice,  $45E_r$  transverse lattice (corresponding to  $U = 413(19)$  Hz at  $14E_r$  longitudinal lattice, where the experiment operates, which agrees with a band-structure calculation of  $401(25)$  Hz). The separation between the resonances as a function of applied gradient is used to calibrate  $E$ . At zero applied magnetic field gradient, we find the stray gradients to be less than  $0.02U$ .

### Local and Long-range Observables

In-situ detection gives the atom number modulo 2 due to light assisted collisions of atoms on each lattice site during imaging. By averaging the occupation of a site over multiple images, we obtain the probability of an odd occupation on the  $j$ th lattice site ( $p_{\text{odd}}^j$ ), which corresponds to the probability of having a single atom on a site within the subspace of our model. This is re-

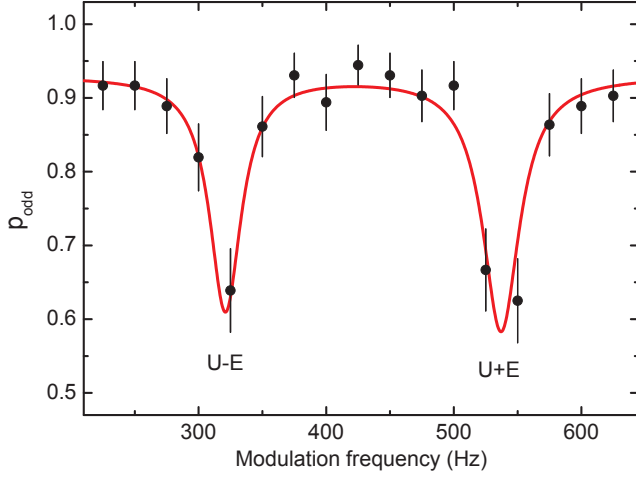


FIG. S8. **Modulation spectroscopy in a tilted lattice.** The occupation probability averaged over the six-site near-homogeneous region described in the main text, plotted versus the modulation frequency, for  $16E_r$  longitudinal lattice modulated by  $\pm 23\%$ , corresponding to a Bose-enhanced resonant tunneling rate[50] of  $2\pi \times 4$  Hz. Because the experiment is performed in a lattice tilted by  $E$  per site, the peak at zero tilt which appears at the interaction energy  $U$  is split out into two peaks, one corresponding to an atom tunneling up the tilt at an energy cost of  $U + E$ , and one to tunneling down the tilt a cost of  $U - E$ . Fitting these peaks allows us to extract both  $U$ , and  $E$ . The peak width arises from a combination of power broadening (approximately  $2\pi \times 14$  Hz, complicated by Rabi flopping), and the residual lattice disorder discussed in the main text.

lated to the spin observables in the effective model by  $\langle S_z^{j-1} S_z^j \rangle = \frac{1}{2} \left( p_{\text{odd}}^j - \frac{1}{2} \right)$ . We average over all the atoms in the chain to obtain  $p_{\text{odd}} = \overline{p_{\text{odd}}^j}$ , which in combination with the constraint that neighboring down spins are not allowed permits us to relate the chain averaged mean  $z$ -projection of spin to  $p_{\text{odd}}$  according to:  $\langle S_z^j \rangle = \frac{p_{\text{odd}}}{2}$ . This quantity varies across the transition and depends only weakly on the chain length. On the other hand, the order parameter for the transition  $O = \left\langle \left( \frac{1}{N} \sum_j (-1)^j S_z^j \right)^2 \right\rangle$  depends on the chain length (Supplementary Fig. S9) and is non-analytic across the transition for a thermodynamic system. The amplitude of the noise correlation signal at separation  $d$  for a chain consisting of a large number of atoms is  $C(d) = 1 + \frac{1}{N^2} \left| \sum_j e^{-i \frac{m a d j}{\hbar t}} n_j \right|^2$  where  $N$  is the number of lattice sites,  $j$  is the lattice site index,  $a$  is the lattice spacing,  $m$  is the mass of the atom,  $t$  is the expansion time,  $n_j$  is the occupation of the  $j$ th site. It can be shown that the correlation signal at  $d = \frac{\pi \hbar t}{m a}$  is related to the order parameter  $O = C \left( \frac{\pi \hbar t}{m a} \right) - 1$ .

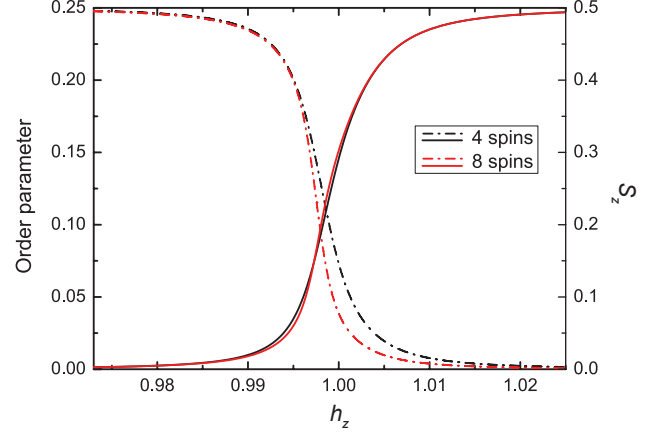


FIG. S9. **Comparing  $S_z$  to the order parameter.** An exact diagonalization calculation (for  $h_x = 0.004$ ) of the ground state of a 1D chain of four (black) and eight (red) Ising spins with nearest-neighbor interactions, revealing that  $S_z$  (solid) is not sensitive to atom number, while the order parameter (dash-dotted) is. It is anticipated that the order parameter will exhibit a cusp in the large-system limit, though the exponential scaling with atom number precludes simulating substantially larger systems on a classical computer.

## Supplementary Information

### Supplementary Discussion of Dark Domain Length Analysis

The magnetic interactions should produce even-length domains of dark sites, corresponding to AF spin domains. To quantify the length of these AF domains we study the length of the measurable dark domains, defining a “dark domain” as a contiguous string of dark sites that is bounded either by a site with an atom or an edge of the region of interest. We then calculate the mean length-weighted dark chain length from this data.

Defects in the initial Mott insulator (MI) reduce the effective system size. Their appearance can produce an overestimate of the dark chain length by either connecting two dark chains, or appearing on the end of a dark chain. The initial MI defect probability is typically 4% per site over an entire  $N = 1$  shell, after correcting for losses during imaging.

Losses and higher order tunneling processes during the ramp can have similar consequences for the observed dark domain length, and can also suppress the observed dark domain length by perturbing atoms near the end of the ramp once the AF has already formed. The rate of such processes can be estimated from the MI  $1/e$  squeezing lifetime in the tilted lattice, measured to be 3.3 seconds. To perform this measurement we first ramp to a tilt of 300 Hz/lattice site and tune the lattice depths to  $45E_r$  and  $14E_r$  for transverse and longitudinal lattices, respec-

tively. We then hold for a variable time, and measure the observed *in situ* atom number. The lifetime is dominated by higher-order tunneling processes. Parametric heating and inelastic scattering become the dominant loss channel in deeper lattices once tunneling is inhibited.

A worst-case estimate for the impact of missing atoms can be reached from the fraction of the time that the system is missing no atoms at the end of the ramp. The six-site chain analyzed in the main text is initially fully occupied 79% of the time. During the time it takes the dark-domain length to grow to 4 lattice sites (60 ms), the aforementioned effects only reduce this number to 73%.

### Supplementary Discussion of Entropy and Thermalization

Supplementary Table 1 shows the entropy per particle ( $S/Nk_B$ ) for several different Mott insulator fidelities ( $p_{\text{odd}}$ ), assuming a chemical potential  $\mu = U/2$ , as well as the mean length-weighted AF domain size  $D$  in an infinite 1D magnetic system with the same entropy per particle. Here  $D = 2(2 - \epsilon)/\epsilon$ , where the spin-dislocation probability in the AF  $\epsilon$  is defined by  $S/Nk_B \approx (\epsilon/2)[1 + \log(1/\epsilon)]$ . Spin defects are ignored as they are both dynamically and thermodynamically unlikely. The entropy per particle can be related to the Mott insulator fidelity by[51]:  $S/Nk_B = \log \left[ \frac{2}{1-p_{\text{odd}}} \right] - p_{\text{odd}} \log \left[ \frac{2p_{\text{odd}}}{1-p_{\text{odd}}} \right]$ . If such thermalization took place in our finite length chain of six sites (with initial fidelity 97.5%), the mean domain size would be limited by the system size to 5.3 sites.

Experimentally, we find most Mott defects to be unbound doublons and holes, which do not directly map to excitations in the spin model. The large energy gap present in our tilted lattice, combined with conservation of particle number, make it difficult for these Mott defects to thermalize with spin degrees of freedom. Such thermalization would require, for example, migration of a doublon to a hole, or decay via a very high order process[34] into several spin defects- quite unlikely within the experimental timescale. Consequently, these nearly static defects act as fixed boundary conditions that limit the effective length of the simulated spin chains. Supplementary Table one also provides the expected uninterrupted chain length, computed as  $L_{\text{sys}} = (1 + p_{\text{odd}})/(1 - p_{\text{odd}})$ .

## Supplementary Discussion of Higher Order Effects

### Interchain Tunneling

Tunneling between chains is excluded from the spin-mapping described in the main text, though under certain conditions it produces exotic transverse superfluidity, as described in Ref. [31]. For our purposes, these tunneling processes serve only to take the system out of the Hilbert space described by the spin model. Most of our experiments were performed at a transverse lattice depth of  $45E_r$ , corresponding to an interchain tunneling rate of  $t_{\text{transverse}} = 2\pi \times 0.07 \text{ Hz}$ . This tunneling rate is basically negligible on our experiment timescale of 250 ms. The noise correlation data, as well as the shell pictures and reversibility curve in Fig. 2 of the main text, were taken at  $35E_r$  transverse lattice depth. At this depth the transverse tunneling rate is  $t_{\text{transverse}} = 2\pi \times 0.27 \text{ Hz}$ , which is small compared to our lattice inhomogeneities, and so results in highly-suppressed, off-resonant Rabi-flopping. In practice, increasing the transverse lattice from  $35E_r$  to  $45E_r$  results in a modest  $\sim 5\%$  improvement in the quality of the Mott insulator after transitioning to the antiferromagnetic state and back.

### Second Order Tunneling

In addition to nearest-neighbor tunneling which creates doublon-hole pairs, and proceeds at a rate  $\sqrt{2}t$  when the tilt  $E = U$ , there remain second-order tunneling processes which create triplons at a rate  $t_{\text{S.O.}} \sim \frac{\sqrt{3}t^2}{U}$ . For our longitudinal lattice depth of  $14E_r$ , and interaction energy  $U = 2\pi \times 416 \text{ Hz}$ , we find  $t_{\text{S.O.}} \sim 2\pi \times 0.4 \text{ Hz}$ .

Because our system is continuously tilted, all such transitions will be tuned through resonance. For our typical experiment,  $R_{\text{ramp}} \approx \frac{\frac{1}{2}U}{250 \text{ ms}} \approx 2\pi \times 840 \text{ Hz}^2$ , so the Landau-Zener adiabatic transition probability to the triplon state  $P_{\text{triplon}} = 1 - \exp \left[ -2\pi \times \frac{t_{\text{S.O.}}^2}{R_{\text{ramp}}} \right] \sim 1\%$ . In future experiments with slower ramps, both this effect and the closely related second-order Stark-shift will become more of a concern. These can be further suppressed relative to the desired dynamics by increasing the longitudinal lattice depth, at the expense of slower many-body dynamics. It bears mentioning that for our experimental parameters the triplon state should experience an additional energy shift calculated to be 22 Hz, due to multi-orbital interactions[52, 53]

### Impact of physics beyond the Hubbard Model

For a  $14E_r$  lattice, the next-nearest neighbor tunneling rate is suppressed relative to that of the nearest neighbor[30] by a factor of  $\sim 300$ , making the total rate  $t_{\text{NextNeighbor}} = 2\pi \times 0.04 \text{ Hz}$ , which is negligible on present experiment timescales. The longitudinal nearest-neighbor interaction shift for one atom per lattice site is  $\sim 10^{-3} \text{ Hz}$ , and interaction driven tunneling[28] occurs with a rate of  $2\pi \times 0.3 \text{ Hz}$ .

Mott Fidelity $p_{\text{odd}}$	Entropy per Particle ( $S/Nk_B$ )	Length-Weighted Mean AF Domain Size (Thermalized)	Length-Weighted Mean Un-interrupted Chain Length (Unthermalized)
0.95	0.23	22	39
0.975	0.13	52	79
0.99	0.063	144	199

TABLE I. For various Mott insulator fidelities, the corresponding configurational entropy per particle is computed. These entropies are comparable to, or well below, the critical entropy for quantum magnetism[34]  $S/Nk_B \sim 0.25 - 0.5$ . If the spin degrees of freedom thermalize efficiently with the Mott degrees of freedom, the spin entropy will then be equal to the Mott entropy. The corresponding mean AF domain size is then computed for each Mott entropy. In the absence of thermalization, the Mott defects break the spin chain into disconnected subsystems, whose mean size is computed in the fourth column, and is comparable to the mean chain length in the presence of thermalization.